ACS APPLIED MATERIALS & INTERFACES

Research Article

www.acsami.org

Monodisperse Fe_3O_4 and γ-Fe_2O_3 Magnetic Mesoporous Microspheres as Anode Materials for Lithium-Ion Batteries

Jing-San Xu and Ying-Jie Zhu*

State Key Laboratory of High Performance Ceramics and Superfine Microstructure, Shanghai Institute of Ceramics, Chinese Academy of Sciences, Shanghai 200050, P. R. China

ABSTRACT: Monodisperse Fe_3O_4 and γ-Fe_2O_3 magnetic mesoporous microspheres are prepared via a surfactant-free solvothermal combined with precursor thermal transformation method. The as-prepared Fe_3O_4 and γ-Fe_2O_3 magnetic mesoporous microspheres have a relatively high specific surface area of 122.3 and 138.6 m^2/g, respectively. The Fe_3O_4 and γ-Fe_2O_3 magnetic mesoporous microspheres are explored as the anode materials for lithium-ion batteries, and they have a high initial discharge capacity of 1307 and 1453 mA h/g, respectively, and a good reversible performance (450 mA h/g for Fe_3O_4 and 697 mA h/g for γ-Fe_2O_3 after 110 cycles) at the current density of 0.2C.

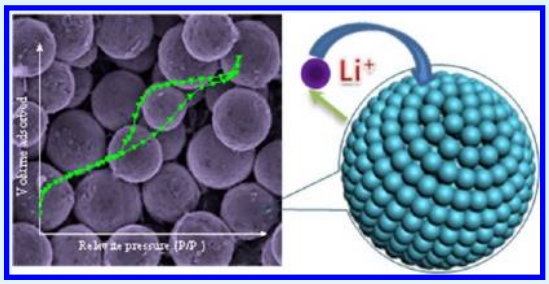

KEYWORDS: *iron oxide, Fe_3O_4, γ-Fe_2O_3, mesoporous, microsphere, magnetic, lithium-ion battery*

INTRODUCTION

The synthesis of mesoporous transition metal oxides is of great significance because of their unique properties and applications in electrochemistry,[1−4] catalysis,[5,6] solar cells,[7,8] etc. Especially, mesoporous materials exhibit excellent electrochemical performances because of their high specific surface areas that can promote the interface contact between electrode and electrolyte, and the mesopores that allow the liquid electrolyte to easily diffuse into the electrode materials, leading to a high flux of lithium ions across the interface and providing space for volume expansion during the discharge and charge processes.[9,10] Usually, mesoporous materials are synthesized with the template-directed methods, adopting the hard templates such as mesoporous silica and carbon[11,12] and the soft templates such as surfactants or long-chain polymers.[13,14] However, multistep procedures are needed in the synthesis and the templates need to be removed from the products, which limit the applications of the methods.

Iron oxides, as one important kind of transition metal oxides, are of great significance due to their wide applications as catalysts,[15−17] electrodes in lithium ion batteries[18,19] and targeted agents in biomedicine.[20,21] Unfortunately, there have been few reports on the fabrication of mesoporous α-Fe_2O_3[22−24] and mesoporous Fe_3O_4.[25−27] The simple surfactant-free preparation of mesoporous iron oxides still remains a challenge.[22,28] Bruce et al.[29] used mesoporous silica as the hard template to synthesize ordered mesoporous Fe_3O_4 and then converted it to mesoporous γ-Fe_2O_3. Zhu et al. reported a simple one-step NaCl-assisted microwave-solvothermal method for the preparation of monodisperse α-Fe_2O_3 mesoporous microspheres,[30] and they also reported a precursor-templated conversion method for the synthesis of Fe_3O_4 or γ-Fe_2O_3 hierarchically nanostructured magnetic hollow microspheres assembled by nanosheets with a relatively high saturation magnetization.[31,32]

Recently, transition metal oxides have been investigated as active anode materials for lithium ion batteries because of their high theoretical specific capacities and the ability to avoid the formation of Li dentrites.[33] The reactions of these compounds with Li^+ ions include the reversible formation and decomposition of Li_2O, which can be described as follows[34]

$$MO_x + 2xLi^+ + 2xe^- \leftrightarrow xLi_2O + M$$

In particular, magnetic iron oxides including Fe_3O_4 and γ-Fe_2O_3 are considered to be promising anode materials for next-generation lithium ion batteries because of their high capacities, environmental friendliness and low cost.[35] However, both Fe_3O_4 and γ-Fe_2O_3 as anode materials usually exhibit poor cyclic performance due to large volume expansion or irreversible phase transformation. Therefore, many recent investigations have focused on the preparation of carbon-coated Fe_3O_4 or γ-Fe_2O_3 to stabilize the structures and thus improve the electrochemical performances.[36−42]

Herein, we report a simple surfactant-free solvothermal combined with precursor thermal transformation method for the synthesis of monodisperse Fe_3O_4 and γ-Fe_2O_3 magnetic mesoporous microspheres. The as-prepared Fe_3O_4 and γ-Fe_2O_3 magnetic mesoporous microspheres have a relatively high specific surface area of 122.3 and 138.6 m^2/g, respectively. The Fe_3O_4 and γ-Fe_2O_3 magnetic mesoporous microspheres are explored as the anode materials for lithium ion batteries without any decoration, and they exhibit a high initial discharge capacity and a good reversible performance.

Received: June 21, 2012
Accepted: August 18, 2012
Published: August 18, 2012

 © 2012 American Chemical Society

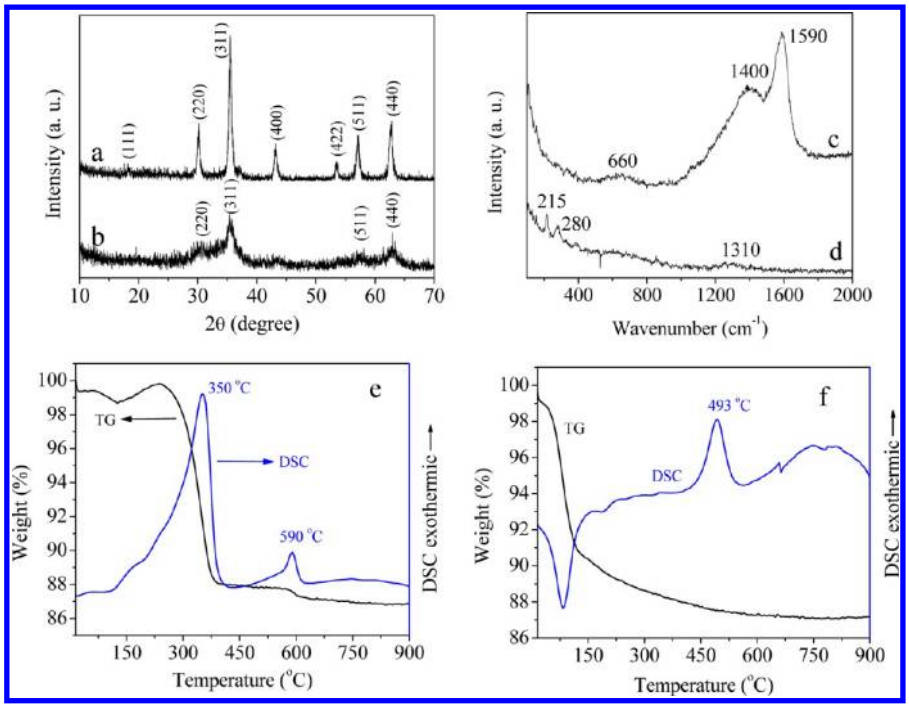

Figure 1. XRD patterns, Raman spectra, and TG and DSC curves of (a, c, e) Fe_3O_4 and (b, d, f) γ-Fe_2O_3 samples.

EXPERIMENTAL SECTION

Preparation of Fe_3O_4 and γ-Fe_2O_3 Magnetic Mesoporous Microspheres. The chemicals used in our experiments were purchased from Sinopharm Chemical Reagent Co., Ltd. and used as received without further purification. The precursor of ferrous tartrate was synthesized according to our previous report[24] with a minor modification. Typically, 0.404 g of $Fe(NO_3)_3{\cdot}9H_2O$ and 0.80 g of tartaric acid were dissolved in 30 mL of dimethylformamide (DMF) under magnetic stirring. The resulting solution was transferred into a 50 mL Teflon lined stainless steel autoclave, sealed, and heated to 160 °C and kept at this temperature for 8 h. After cooling to room temperature naturally, the product was collected by centrifugation, washed with ethanol, and dried to powder as the precursor at 60 °C.

For the preparation of Fe_3O_4 mesoporous microspheres, the ferrous tartrate precursor powder was heated at 400 °C h in flowing nitrogen gas for 1 h. γ-Fe_2O_3 mesoporous microspheres were obtained by heat treatment of the ferrous tartrate precursor powder at 320 °C in air for 1 h.

Materials Characterization. X-ray powder diffraction (XRD) patterns of the as-prepared samples were recorded using a Rigaku D/Max 2550 V X-ray diffractometer with a high-intensity Cu−K_α radiation (λ = 1.54178 Å). Raman spectra were taken on a DXR Raman Microscope (Thermo Scientific). Thermogravimetric (TG) and differential scanning calorimetric (DSC) curves were measured on a STA 409/PC simultaneous thermal analyzer (Netzsch, Germany) with a heating rate of 10 °C min^{-1} in flowing air. Scanning electron microscopy (SEM) micrographs were obtained on a Hitachi S-4800 field-emission scanning electron microscope. Transmission electron microscopy (TEM) micrographs were carried out with a JEOL JEM-2100F field-emission transmission electron microscope. The Brunauer-Emmett-Teller (BET) specific surface area and pore size distribution were measured with a surface area and pore size analyzer (V-sorb 2800P, Gold APP Instruments, China). A physical property measurement system (PPMS, Quantum Design, USA) was used to evaluate the magnetic properties of the samples at 300 and 5 K.

Electrochemical Measurements. The working electrode for electrochemical measurements was prepared by dispersing the as-synthesized active material, acetylene black and polyvinylidene difuoride (PVDF) at the weight percent ratio of 75:15:10 in the solvent of N-methyl-2-pyrrolidone (NMP). Then the slurry was cast on a copper foil using automatic film-coating equipment and dried at 120 °C for 8 h in vacuum. 2025 coin cells were assembled using Celgard 2400 as separator, lithium foil as counter and reference electrode, and 1 M $LiPF_6$ in mixed solvents of ethylene carbonate (EC) and diethylcarbonate (DEC) (weight ratio = 1:1) as electrolyte. The assembly of cells was processed in an argon filled glove box with oxygen and water contents less than 1 ppm. The galvanostatic charge/discharge tests were conducted on a LAND CT2001A battery test system in a voltage range of 0.01−3.0 V (versus Li/Li^+) at a current density of 0.2 C (185 mA/g for Fe_3O_4 and 201 mA/g for γ-Fe_2O_3).

RESULTS AND DISCUSSION

The XRD pattern of the as-prepared Fe_3O_4 product is shown in Figure 1a, the diffraction peaks can be indexed to single-phase Fe_3O_4 (JCPDS No. 85-1436). Figure 1b shows the XRD pattern of the γ-Fe_2O_3 sample, which can be indexed to γ-Fe_2O_3 (JCPDS no. 39-1346), and the crystallinity of γ-Fe_2O_3 was low because of the low heat-treatment temperature.

Raman spectra were employed to investigate the composition of the Fe_3O_4 and γ-Fe_2O_3 samples. As shown in Figure 1c, the Raman spectrum of the Fe_3O_4 sample has a broad weak band centered at around 660 cm^{-1}, corresponding to the A_{1g} mode of Fe_3O_4. Also two peaks at about 1393 and 1590 cm^{-1} appear, which can be attributed to the fundamental D and G bands of carbon, respectively. The presence of carbon may be explained by the carbonization of organic constituents in the precursor during subsequent heat treatment, and was further confirmed by the TG analysis. The Raman spectrum of the γ-Fe_2O_3 sample shown in Figure 1d exhibits two small peaks at 215 and 285 cm^{-1}, which can be assigned as the A_{1g} mode and E_g mode of the α-Fe_2O_3 phase, respectively. This should be explained by the degradation of γ-Fe_2O_3 to α-Fe_2O_3 induced by the laser irradiation, and the broad peak located at around 1310 cm^{-1} can be ascribed to γ-Fe_2O_3.[43]

Panels e and f in Figure 1 show the TG and DSC curves of Fe_3O_4 and γ-Fe_2O_3 samples measured under the air atmosphere. For the Fe_3O_4 sample, the weight increase between 125 and 235 °C was caused by the oxidation of

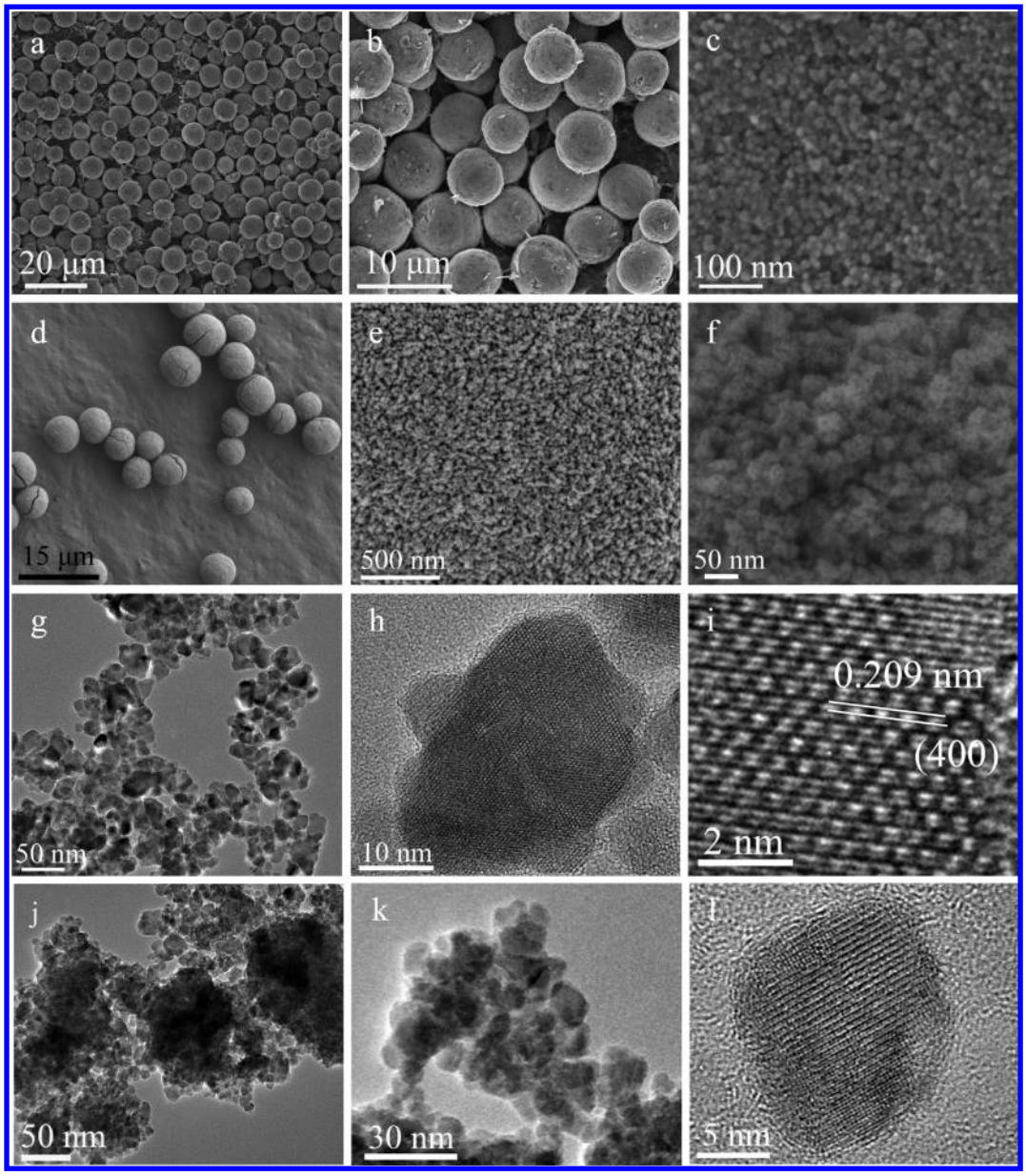

Figure 2. (a–f) SEM micrographs: (a, b) Fe_3O_4 mesoporous microspheres, and (c) the surface of an individual Fe_3O_4 microsphere; (d) γ-Fe_2O_3 mesoporous microspheres, and (e, f) the surface of an individual γ-Fe_2O_3 microsphere. (g–l) TEM micrographs: (g–i) nanoparticles obtained by grinding Fe_3O_4 mesoporous microspheres; and (j–l) nanoparticles obtained by grinding γ-Fe_2O_3 mesoporous microspheres.

Fe_3O_4 to form γ-Fe_2O_3, and after that, the TG curve exhibited two weight loss stages, as shown in Figure 1e. The first stage, beginning from 240 to 400 °C with an exothermic peak at about 350 °C can be ascribed to the decomposition of the residual organic molecules. And another small one, from 500 to 650 °C with an exothermic peak at about 590 °C is assigned to the oxidation of carbon formed during the heat treatment process. Figure 1f shows the TG and DSC curves of the γ-Fe_2O_3 sample. The weight loss below 130 °C resulted from the evaporation of the adsorbed water. The weight loss from 140 to 600 °C should be attributed to the removal of the residual organics with an obvious exothermic peak at about 493 °C.

The morphologies of the Fe_3O_4 and γ-Fe_2O_3 samples were investigated with SEM and TEM, as shown in Figure 2. From images a and b in Figure 2, one can see that the Fe_3O_4 sample was composed of monodisperse microspheres with an average diameter of ~6 μm. The high-magnification image (Figure 2c) clearly shows that the individual Fe_3O_4 microsphere was composed of a large number of nanoparticles, and these nanoparticles were self-assembled to form the three-dimensional mesoporous network. To verify this point, we ground the powder of Fe_3O_4 mesoporous microspheres with the mortar and pestle, and the obtained powder was dispersed in ethanol and observed with TEM (Figure 2g–i). The TEM image in Figure 2g exhibits irregularly shaped nanoparticles with the sizes ranging from 10 to 30 nm. Figure 2h shows an individual nanoparticle. Figure 2i shows the corresponding high-resolution TEM (HRTEM) image, exhibiting the lattice fringes that can be attributed to the (400) planes of Fe_3O_4 with a cubic structure. Figure 2d–f shows the SEM micrographs of the γ-Fe_2O_3 product, which are similar to those of Fe_3O_4 mesoporous microspheres. However, the cracks in γ-Fe_2O_3 mesoporous microspheres were observed while Fe_3O_4 mesoporous microspheres were unbroken. Besides, the nanoparticles obtained by

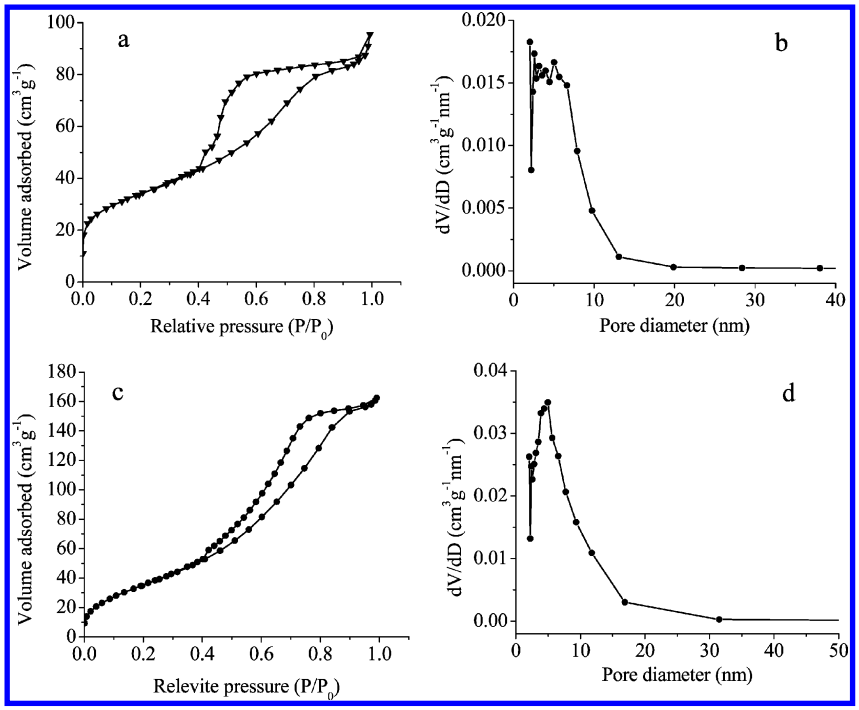

Figure 3. N_2 adsorption−desorption isotherms and BJH−adsorption pore size distributions of magnetic mesoporous microspheres: (a, b) Fe_3O_4 and (c, d) γ-Fe_2O_3.

grinding γ-Fe_2O_3 mesoporous microspheres were also studied by TEM, as shown in Figure 2j−l. The sizes of the γ-Fe_2O_3 nanoparticles were smaller than those of Fe_3O_4 nanoparticles. Figure 2l shows an individual γ-Fe_2O_3 nanocrystal with a size of ∼10 nm.

In our previous paper,[24] we proposed the formation mechanism for the microspheres of the precursor of ferrous tartrate. By adopting a thermal treatment method under different environments, the microspheres of the precursor of ferrous tartrate can be transformed to Fe_3O_4 and γ-Fe_2O_3 magnetic mesoporous microspheres, respectively. The organic constituents in the precursor of ferrous tartrate decompose at elevated temperatures (320 or 400 °C) in air or flowing nitrogen during the thermal transformation process. After the removal of the organic constituents in the precursor of ferrous tartrate, the microspheres of the precursor are transformed to Fe_3O_4 or γ-Fe_2O_3 microspheres, and at the same time mesopores form in the microspheres. The transformation of the precursor to Fe_3O_4 or γ-Fe_2O_3 can be described using the following chemical equations

$$4C_4H_4O_6Fe + 11O_2 \rightarrow 2Fe_2O_3 + 16CO_2 + 8H_2O$$

$$C_4H_4O_6Fe \rightarrow Fe_3O_4 + CO_2 + H_2O$$

Figure 3 shows the N_2 adsorption−desorption isotherms and corresponding Barrett-Joyner-Halenda (BJH) pore size distribution plots of as-prepared Fe_3O_4 and γ-Fe_2O_3 mesoporous microspheres. Large hysteresis loops which resemble typical H1-type isotherms were observed for both Fe_3O_4 and γ-Fe_2O_3 samples. The Brunauer-Emmett-Teller (BET) specific surface areas of Fe_3O_4 and γ-Fe_2O_3 mesoporous microspheres were measured to be 122.3 and 138.6 m^2/g, respectively, which are higher than those reported previously.[27,29,44,45] The BJH average pore diameter calculated from the adsorption branch of the isotherms was 5.9 and 6.1 nm for the Fe_3O_4 and γ-Fe_2O_3 samples, respectively, and the corresponding total pore volume was 0.13 and 0.27 cm^3/g, respectively.

The magnetic properties of as-prepared Fe_3O_4 and γ-Fe_2O_3 mesoporous microspheres were investigated at 300 and 5 K in the applied magnetic field from −20 to 20 kOe. The magnetic hysteresis loops and the enlarged low-field hysteresis (inset) of Fe_3O_4 and γ-Fe_2O_3 mesoporous microspheres are shown in Figure 4. The curves shown in Figure 4a indicate that Fe_3O_4 mesoporous microspheres had a high saturation magnetization

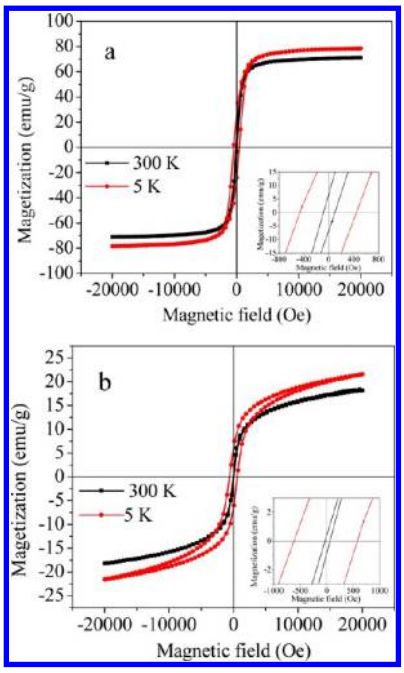

Figure 4. Magnetic hysteresis loops of (a) Fe_3O_4 and (b) γ-Fe_2O_3 mesoporous microspheres at 300 and 5 K.

(M_s) of 71.0 emu/g at the temperature of 300 K, and the remnant magnetization (M_r) and coercivity (H_c) were determined to be 6.7 emu/g and 92.0 Oe, respectively. When the temperature decreased to 5 K, the value of M_s increased to 78.5 emu/g, and M_r and H_c significantly increased to 24.6 emu/g and 455.1 Oe, respectively. For γ-Fe_2O_3 mesoporous microspheres, no saturation of magnetization was observed at both 300 and 5 K. The magnetization values at the maximum magnetic field of 20 kOe were 18.2 and 21.6 emu/g at 300 and 5 K, respectively. Notably, the H_c value dramatically increased from 47.3 to 599.2 Oe when the temperature declined from 300 K to 5 K, which is even higher than that of the Fe_3O_4 sample.

Fe_3O_4 and γ-Fe_2O_3 mesoporous microspheres were evaluated for reversible Li ion storage at a current density of 0.2*C* (185 mA/g for Fe_3O_4 and 201 mA/g for γ-Fe_2O_3) in the voltage window of 0.01−3.0 V. Panels a and b in Figure 5 show the corresponding voltage profiles and Figure 5c shows the discharge capacity as well as Coulombic efficiency of Fe_3O_4 and γ-Fe_2O_3 mesoporous microspheres. According to previous works,[34,41] the reversible electrochemical reactions in the lithium ion batteries can be described as follows

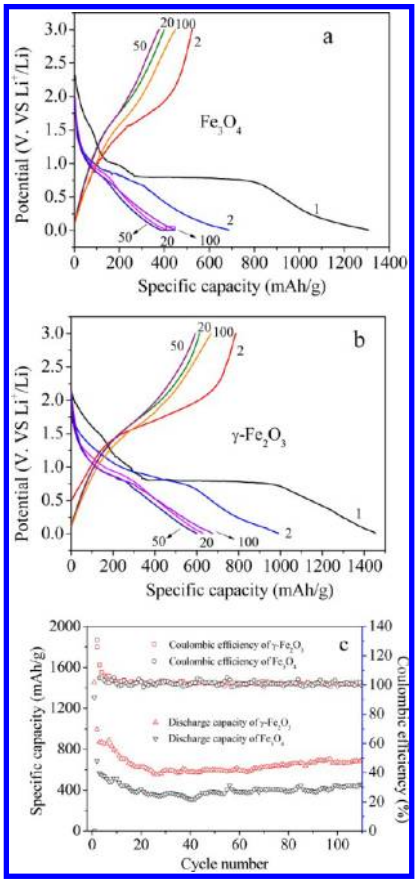

Figure 5. (a, b) 1st, 2nd, 20th, 50th, and 100th charge−discharge curves; (c) discharge capacity as well as Coulombic efficiency versus cycle number for Fe_3O_4 and γ-Fe_2O_3 mesoporous microspheres.

$$Fe_3O_4 + 8Li^+ + 8e^- \leftrightarrow 4Li_2O + 3Fe$$

$$Fe_2O_3 + 6Li^+ + 6e^- \leftrightarrow 3Li_2O + 2Fe$$

On the basis of the two redox reactions, the theoretical capacity of Fe_3O_4 and γ-Fe_2O_3 is 924 and 1007 mA h/g, respectively. However, the initial specific discharge capacity of the as-prepared Fe_3O_4 and γ-Fe_2O_3 mesoporous microspheres was 1307 and 1453 mA h/g, respectively, which is much higher than the theoretical value. This kind of phenomenon can be ascribed to the reversible formation and decomposition of a polymeric gel-like film on the surface of the electrode particles.[46,47] This film arises from the kinetically governed electrolyte degradation driven by the active metal nanoparticles (Fe). The cycling performances of both Fe_3O_4 and γ-Fe_2O_3 samples were investigated up to 110 cycles. It has been found that both Fe_3O_4 and γ-Fe_2O_3 mesoporous microspheres show perfect coulombic efficiencies after the first discharge process. For the Fe_3O_4 sample, the specific capacity dropped to 312 mA h/g after the first 40 cycles, and then it increased gradually to about 450 mA h/g after 110 cycles. In contrast, γ-Fe_2O_3 mesoporous microspheres exhibited a capacity of 871 mA h/g at the 3rd cycle and decreased to a minimum value of 553 mA h/g at the 27th cycle. The capacity degradation resulted from the large volume changes of Fe_3O_4 and γ-Fe_2O_3 mesoporous microspheres after the lithium insertion. However, after that the capacity showed an increasing trend and reached 697 mA h/g at the 110th cycle. The result of initial drop followed by gradual rise of the capacity has been widely reported for transition metal oxide electrodes and can be attributed to the reversible growth of the gel-like polymer layer that wraps the nanoparticles of the electrode.[37,46] Although the specific capacity of the γ-Fe_2O_3 mesoporous microspheres exhibited some fluctuations during cycling and was lower than that of some other carbon-coated iron oxides,[39,40] the value was still higher than many reports.[41,48−50] We propose that the high capacity roots in high specific surface area and mesoporous structure of the as-prepared Fe_3O_4 and γ-Fe_2O_3 mesoporous microspheres, which promote the contact between the electrode and electrolyte.

■ CONCLUSIONS

A surfactant-free solvothermal combined with precursor thermal transformation method has been demonstrated for the synthesis of monodisperse Fe_3O_4 and γ-Fe_2O_3 magnetic mesoporous microspheres. Firstly, a surfactant-free solvothermal method is adopted to prepare the microspheres of the precursor of ferrous tartrate ($C_4H_4O_6Fe$) using $Fe(NO_3)_3$ and tartaric acid in the solvent of dimethylformamide (DMF) at 160 °C for 8 h. Secondly, the precursor powder is transformed by heat treatment to Fe_3O_4 and γ-Fe_2O_3 magnetic mesoporous microspheres at 400 and 320 °C for 1 h in nitrogen gas and air, respectively. The as-prepared Fe_3O_4 and γ-Fe_2O_3 magnetic mesoporous microspheres have a relatively high specific surface area of 122.3 and 138.6 m^2/g, respectively, and Fe_3O_4 mesoporous microspheres show a high saturation magnetization (71.0 emu/g at 300 K and 78.5 emu/g at 5 K). The as-prepared Fe_3O_4 and γ-Fe_2O_3 magnetic mesoporous microspheres are promising anode materials for lithium ion batteries, and they have a high initial discharge capacity of 1307 and 1453 mAh/g, respectively, and a good reversible performance (450 mA h/g for Fe_3O_4 and 697 mA h/g for γ-Fe_2O_3 after 110 cycles) at the current density of 0.2*C*.

■ AUTHOR INFORMATION

Corresponding Author

*Tel: 86-21-52412616. Fax: 86-21-52413122. E-mail: y.j.zhu@mail.sic.ac.cn.

Notes

The authors declare no competing financial interest.

■ ACKNOWLEDGMENTS

Financial support from the National Natural Science Foundation of China (51172260, 51121064), the Science and Technology Commission of Shanghai (11nm0506600, 1052nm06200), and CAS/SAFEA International Partnership Program for Creative Research Teams is gratefully acknowledged.

■ REFERENCES

(1) Li, Y.; Tan, B.; Wu, Y. *Nano Lett.* **2007**, *8*, 265.
(2) Jiao, F.; Bruce, P. G. *Adv. Mater.* **2007**, *19*, 657.
(3) Kim, H.; Cho, J. *J. Mater. Chem.* **2008**, *18*, 771.
(4) Ren, Y.; Hardwick, L. J.; Bruce, P. G. *Angew. Chem., Int. Ed.* **2010**, *49*, 2570.
(5) Ho, C.; Yu, J. C.; Kwong, T.; Mak, A. C.; Lai, S. *Chem. Mater.* **2005**, *17*, 4514.
(6) Bian, Z.; Zhu, J.; Cao, F.; Huo, Y.; Lu, Y.; Li, H. *Chem. Commun.* **2010**, *46*, 8451.
(7) Ito, S.; Makari, Y.; Kitamura, T.; Wada, Y.; Yanagida, S. *J. Mater. Chem.* **2004**, *14*, 385.
(8) Huang, F.; Chen, D.; Zhang, X. L.; Caruso, R. A.; Cheng, Y.-B. *Adv. Funct. Mater.* **2010**, *20*, 1301.
(9) Bruce, P. G.; Scrosati, B.; Tarascon, J.-M. *Angew. Chem., Int. Ed.* **2008**, *47*, 2930.
(10) Fang, X.; Yu, X.; Liao, S.; Shi, Y.; Hu, Y.-S.; Wang, Z.; Stucky, G. D.; Chen, L. *Microporous Mesoporous Mater.* **2012**, *151*, 418.
(11) Lu, A. H.; Schüth, F. *Adv. Mater.* **2006**, *18*, 1793.
(12) Rumplecker, A.; Kleitz, F.; Salabas, E.-L.; Schüth, F. *Chem. Mater.* **2007**, *19*, 485.
(13) Yang, P.; Zhao, D.; Margolese, D. I.; Chmelka, B. F.; Stucky, G. D. *Chem. Mater.* **1999**, *11*, 2813.
(14) Fan, J.; Boettcher, S. W.; Stucky, G. D. *Chem. Mater.* **2006**, *18*, 6391.
(15) Cao, S. W.; Zhu, Y. J. *J. Phys. Chem. C* **2008**, *112*, 6253.
(16) Tahir, A. A.; Wijayantha, K. G. U.; Saremi-Yarahmadi, S.; Mazhar, M.; McKee, V. *Chem. Mater.* **2009**, *21*, 3763.
(17) Zhang, Z.; Hossain, M. F.; Takahashi, T. *Appl. Catal. B: Environ.* **2010**, *95*, 423.
(18) Muraliganth, T.; Vadivel Murugan, A.; Manthiram, A. *Chem. Commun.* **2009**, 7360.
(19) Wang, B.; Chen, J. S.; Wu, H. B.; Wang, Z.; Lou, X. W. *J. Am. Chem. Soc.* **2011**, *133*, 17146.
(20) Zhang, J.; Misra, R. D. K. *Acta Biomater.* **2007**, *3*, 838.
(21) Tartaj, P.; Morales, M. P.; Gonzalez-Carreño, T.; Veintemillas-Verdaguer, S.; Serna, C. J. *Adv. Mater.* **2011**, *23*, 5243.
(22) Jiao, F.; Bruce, P. G. *Angew. Chem., Int. Ed.* **2004**, *43*, 5958.
(23) Mao, D.; Yao, J.; Lai, X.; Yang, M.; Du, J.; Wang, D. *Small* **2011**, *7*, 578.
(24) Xu, J. S.; Zhu, Y. J. *CrystEngComm* **2012**, *14*, 2702.
(25) Liu, X.; Guo, Y.; Wang, Y.; Ren, J.; Wang, Y.; Guo, Y.; Guo, Y.; Lu, G.; Wang, Y.; Zhang, Z. *J. Mater. Sci.* **2010**, *45*, 906.
(26) Chen, L.; Lin, Z.; Zhao, C.; Zheng, Y.; Zhou, Y.; Peng, H. *J. Alloys Compd.* **2011**, *509*, L1.
(27) Tüysüz, H.; Weidenthaler, C.; Schüth, F. *Chem.—Eur. J.* **2012**, *18*, 5080.
(28) Brezesinski, T.; Groenewolt, M.; Antonietti, M.; Smarsly, B. *Angew. Chem., Int. Ed.* **2006**, *45*, 781.
(29) Jiao, F.; Jumas, J.-C.; Womes, M.; Chadwick, A. V.; Harrison, A.; Bruce, P. G. *J. Am. Chem. Soc.* **2006**, *128*, 12905.
(30) Cao, S. W.; Zhu, Y. J. *Nanoscale Res. Lett.* **2011**, *6*, No. Art. No.1.
(31) Cao, S. W.; Zhu, Y. J.; Ma, M. Y.; Li, L.; Zhang, L. *J. Phys. Chem. C* **2008**, *112*, 1851.
(32) Cao, S. W.; Zhu, Y. J. *J. Phys. Chem. C* **2008**, *112*, 12149.
(33) Kanzaki, S.; Inada, T.; Matsumura, T.; Sonoyama, N.; Yamada, A.; Takano, M.; Kanno, R. *J. Power Sources* **2005**, *146*, 323.
(34) Poizot, P.; Laruelle, S.; Grugeon, S.; Dupont, L.; Tarascon, J. M. *Nature* **2000**, *407*, 496.
(35) Mitra, S.; Poizot, P.; Finke, A.; Tarascon, J. M. *Adv. Funct. Mater.* **2006**, *16*, 2281.
(36) Chou, S.-L.; Wang, J.-Z.; Wexler, D.; Konstantinov, K.; Zhong, C.; Liu, H.-K.; Dou, S.-X. *J. Mater. Chem.* **2010**, *20*, 2092.
(37) Wu, P.; Du, N.; Zhang, H.; Yu, J.; Yang, D. *J. Phys. Chem. C* **2011**, *115*, 3612.
(38) Ma, Y.; Ji, G.; Lee, J. Y. *J. Mater. Chem.* **2011**, *21*, 13009.
(39) Zhu, T.; Chen, J. S.; Lou, X. W. *J. Phys. Chem. C* **2011**, *115*, 9814.
(40) Yuan, S. M.; Li, J. X.; Yang, L. T.; Su, L. W.; Liu, L.; Zhou, Z. *ACS Appl. Mater. Interfaces* **2011**, *3*, 705.
(41) Yuan, S. M.; Zhou, Z.; Li, G. *CrystEngComm* **2011**, *13*, 4709.
(42) Su, L. W.; Jing, Y.; Zhou, Z. *Nanoscale* **2011**, *3*, 3967.
(43) Varadwaj, K. S. K.; Panigrahi, M. K.; Ghose, J. *J. Solid State Chem.* **2004**, *177*, 4286.
(44) Wang, P.; Lo, I. M. C. *Water Res.* **2009**, *43*, 3727.
(45) Zhang, S. F.; Wu, W.; Xiao, X. H.; Zhou, J.; Ren, F.; Jiang, C. Z. *Nanoscale Res. Lett.* **2011**, *6*, No. Art.No. 89.
(46) Grugeon, S.; Laruelle, S.; Dupont, L.; Tarascon, J. M. *Solid State Sci.* **2003**, *5*, 895.
(47) Yu, Y.; Chen, C.-H.; Shui, J.-L.; Xie, S. *Angew. Chem., Int. Ed.* **2005**, *44*, 7085.
(48) Kanzaki, S.; Yamada, A.; Kanno, R. *J. Power Sources* **2007**, *165*, 403.
(49) Manuel, J.; Kim, J.-K.; Ahn, J.-H.; Cheruvally, G.; Chauhan, G. S.; Choi, J.-W.; Kim, K.-W. *J. Power Sources* **2008**, *184*, 527.
(50) Nagao, M.; Otani, M.; Tomita, H.; Kanzaki, S.; Yamada, A.; Kanno, R. *J. Power Sources* **2011**, *196*, 4741.